

Article

Effect of Yttrium on Ce/Ni-Metakaolin Catalysts for CO₂ Methanation

Yuyi Wang¹, Quan Ye¹, Xinyu Xu¹, Abdelghaffar S. Dhmees²  and Xuemin Cui^{1,*}

¹ Guangxi Key Lab of Petrochemical Resource Processing and Process Intensification Technology, School of Chemistry and Chemical Engineering, Guangxi University, Nanning 530004, China; 2114931095@st.gxu.edu.cn (Y.W.); ye-q@st.gxu.edu.cn (Q.Y.); wang-yy@st.gxu.edu.cn (X.X.)

² Egyptian Petroleum Research Institute, Ahmed El-Zomor St., Nasr City, Cairo 11727, Egypt; abdel_ghffar@yahoo.com

* Correspondence: cuixm@gxu.edu.cn

Abstract: In recent years, major economies have implemented carbon reduction and carbon neutrality policies. Furthermore, with advancements in science and technology, carbon dioxide (CO₂) is now considered a valuable raw material for producing carbon-based fuels through hydrogenation. Various concentrations of yttrium (referred to as Y hereafter) were introduced to assess their influence on the catalytic performance of CO₂ methanation. At a temperature of 300 °C, the catalyst exhibited an impressive CO₂ conversion rate of 78.4% and maintained remarkable stability throughout a rigorous 100 h stability assessment. The findings suggest that the inclusion of yttrium (Y) promotes the formation of oxygen vacancies and alkaline sites on the catalyst. This, in turn, enhances the reducibility of nickel species, improves the dispersion of nickel particles, and plays a pivotal role in enhancing thermal stability. Furthermore, it offers an innovative design approach for creating highly efficient composite CO₂ methanation catalysts by controlling particle size and harnessing synergistic catalytic effects at the metal/support interface.

Keywords: CO₂; methanation; metakaolin; catalyst; multiple metals



Citation: Wang, Y.; Ye, Q.; Xu, X.; Dhmees, A.S.; Cui, X. Effect of Yttrium on Ce/Ni-Metakaolin Catalysts for CO₂ Methanation. *Molecules* **2023**, *28*, 7079. <https://doi.org/10.3390/molecules28207079>

Academic Editor: Xiaohuan Liu

Received: 17 September 2023

Revised: 8 October 2023

Accepted: 11 October 2023

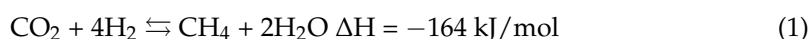
Published: 13 October 2023



Copyright: © 2023 by the authors. Licensee MDPI, Basel, Switzerland. This article is an open access article distributed under the terms and conditions of the Creative Commons Attribution (CC BY) license (<https://creativecommons.org/licenses/by/4.0/>).

1. Introduction

The intensifying Russo–Ukrainian conflict has exacerbated global warming and energy shortages, emphasizing the imperative to tackle the ongoing increase in atmospheric CO₂ levels caused by persistent fossil fuel consumption [1]. Considering CO₂'s abundance and cost-effectiveness as a source of carbon and oxygen, there has been a growing impetus to transform CO₂ into value-added products, thereby mitigating CO₂ emissions [2]. Academic and industrial research in the field of CO₂ catalytic hydrogenation is continuously advancing and garnering escalating global interest [3]. CO₂ hydrogenation presents the potential to produce a diverse array of chemical compounds, such as methane, ethanol, and ethylene [4]. Methane, among these compounds, stands out as a highly promising and widely utilized energy resource [5], rendering the thermodynamically significant CO₂ methanation reaction of particular significance. In the exhaust gases, CO₂ captured and renewable H₂ undergo a catalytic Sabatier reaction during combustion to produce synthetic methane [6].



Over the past few decades, significant time and effort have been devoted worldwide on CO₂ methanation, with numerous publications reporting on the potential of CO₂ methanation catalyzed by Ru, Rh, Co, Ni, etc. [7–10]. Precious metal catalysts manifest remarkable catalytic performance and enhanced specificity for CH₄. Nonetheless, the high cost of noble metals and their excessively high sintering temperatures have hindered their widespread application, making it challenging to meet the demands of industrial-scale production.

Consequently, there has been a growing exploration for low-cost and abundantly available non-noble metal catalysts. The overall efficacy of catalysts is influenced not solely by the active metal, but the characteristics of the support also significantly affect the catalyst's performance, as they are instrumental in shaping its structure, promoting even distribution, and facilitating the reduction in the metal phase [11,12].

Nickel-based catalysts have garnered significant research interest as a viable substitution for precious metal catalysts in the CO₂ methanation process, owing to their cost-effectiveness, remarkable activity, and selectivity [13]. At elevated temperatures, nickel-based catalysts, despite their advantages, exhibit susceptibility to carbon deposition and sintering, thus leading to rapid deactivation, and their performance at low temperatures also requires improvement [14]. Consequently, in recent years, the research focus on CO₂ methanation catalysts has shifted to inhibiting deactivation, exploring promoters, and enhancing low-temperature activity.

Catalyst supports have a vital function in stabilizing the catalyst and preventing the aggregation of active metals. Widely employed supports for CO₂ methanation catalysts encompass TiO₂ [15], Al₂O₃ [16], ZrO₂ [17], and others, but these supports are chemically synthesized materials. To introduce a low-cost and environmentally friendly catalyst support, metakaolin, derived from kaolin clay through dehydration at appropriate temperatures (600–900 °C), is an attractive material. Metakaolin, abbreviated as MK, is an activated aluminosilicate (Al₂O₃ · 2SiO₂) and serves as a highly active mineral admixture. Mesoporous solids can be used in the separation of complex mixtures of organic molecules in addition to the proposed use as catalysts in reactions such as CO₂ methanation [18]. Novia Amalia Sholeha et al. [19] examined the synthesis of nickel catalysts utilizing dealuminated metakaolin zeolite as a supporting material. Metakaolin is not only affordable and readily available but also environmentally friendly, being a clay mineral [20] that facilitates CO₂ adsorption. Additionally, it exhibits high Al₂O₃ and SiO₂ content, making it a promising candidate as a support for CO₂ hydrogenation catalysts.

In recent years, CeO₂ has often been introduced as a second metal in nickel-based catalysts for its notable catalytic enhancing effect in the CO₂ methanation process. Li et al. [21] uncovered that the incorporation of CeO₂ suppresses the coalescence of nickel particles and promotes synergy between the active metal and the substrate, thereby enhancing the catalytic effectiveness of Ni catalysts containing nickel. While Ce has attracted attention as a promising promoter when incorporated into nickel-based catalysts for methane conversion, other promoters such as Mg [22,23], Y [24], and Zr [25,26] have also been widely applied for the enhancement of nickel-based catalysts. Researchers have highlighted that Y-doped catalysts based on nickel exhibit dual advantages. They not only enhance the BET surface area, facilitating the creation of weakly basic and moderately basic sites, but also reduce the particle size of nickel, promoting better dispersion. Consequently, Y has demonstrated remarkable efficacy as a catalyst enhancer in the CO₂ methanation process. It exhibits exceptional promotional properties for catalysts relying on nickel as their active component [27,28]. Furthermore, studies have indicated that Y-modified Co/TiO₂ enhances the CO₂ capture capacity and surface basicity of the catalyst's active species, thus enhancing the catalyst's activity [29]. Investigations were conducted on Ni-based catalysts doped with Ce-Zr or Ce-Y promoters for various reactions, including methane reforming and methane dry reforming [30,31]. The outcomes reveal that Ni catalysts co-doped with both promoters exhibit enhanced catalytic activity. Nevertheless, previous research primarily focused on Ni-based catalysts modified with only one promoter. Therefore, in pursuit of a highly efficient catalyst, this study incorporates Ce-Y promoters into metakaolin-based nickel catalysts.

To date, there have been no reports on the impact of Ce-Y promotion on the structure, morphology, and CO₂ conversion rate of nickel-supported metakaolin catalysts in the CO₂ methanation process.

This knowledge gap necessitates the design of catalysts with superior performance in CO₂ methanation. This study proposes the utilization of cost-effective, readily available and

environmentally friendly metakaolin (MK) as catalyst support. Through a co-impregnation method, Y-Ce/Ni-MK catalysts with a fixed Ni and Ce concentration of 15 wt.% and varying Y loadings (1, 3, and 5 wt.%) were synthesized. Multiple characterization methodologies were utilized to investigate the correlation between catalyst activity and its structure, as well as physicochemical properties. The performance and durability of the Y-Ce/Ni-MK catalysts were explored using a combined gas chromatograph and fixed-bed reactor approach. This investigation explores the impact of Y incorporation on the effectiveness of Ce/Ni-MK catalysts and investigates the synergistic effects arising from the interaction of Y with Ce, and the mechanistic aspects of CO₂ methanation catalyzed by Y-Ce/Ni-MK catalysts were thoroughly examined.

2. Results

2.1. Structure of the Catalysts

As shown in Figure 1, Y-Ce/Ni-MK, Ce/Ni-MK, and Ni-MK all demonstrate type IV adsorption characteristics accompanied by H3-type hysteresis patterns, suggesting the existence of mesoporous architectures in the three catalysts. Data in Table 1 clearly displays that Y-Ce/Ni-MK catalyst outperforms the other two catalysts in terms of specific surface area and pore volume. Due to the existence of mesoporous structures in the catalysts, the cavities within the substrate may experience partial obstruction by Ni following the introduction of the promoter, leading to a marginal decrease in pore dimension for Y-Ce/Ni-MK and Ce/Ni-MK in comparison to Ni-MK.

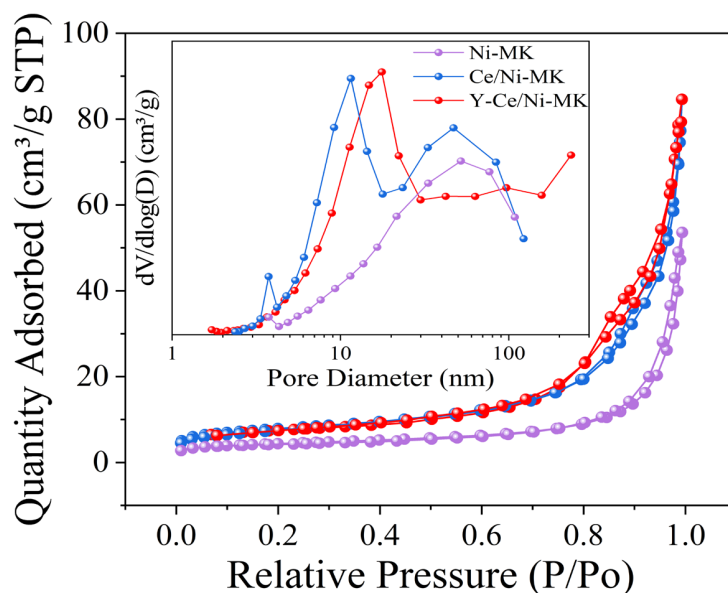
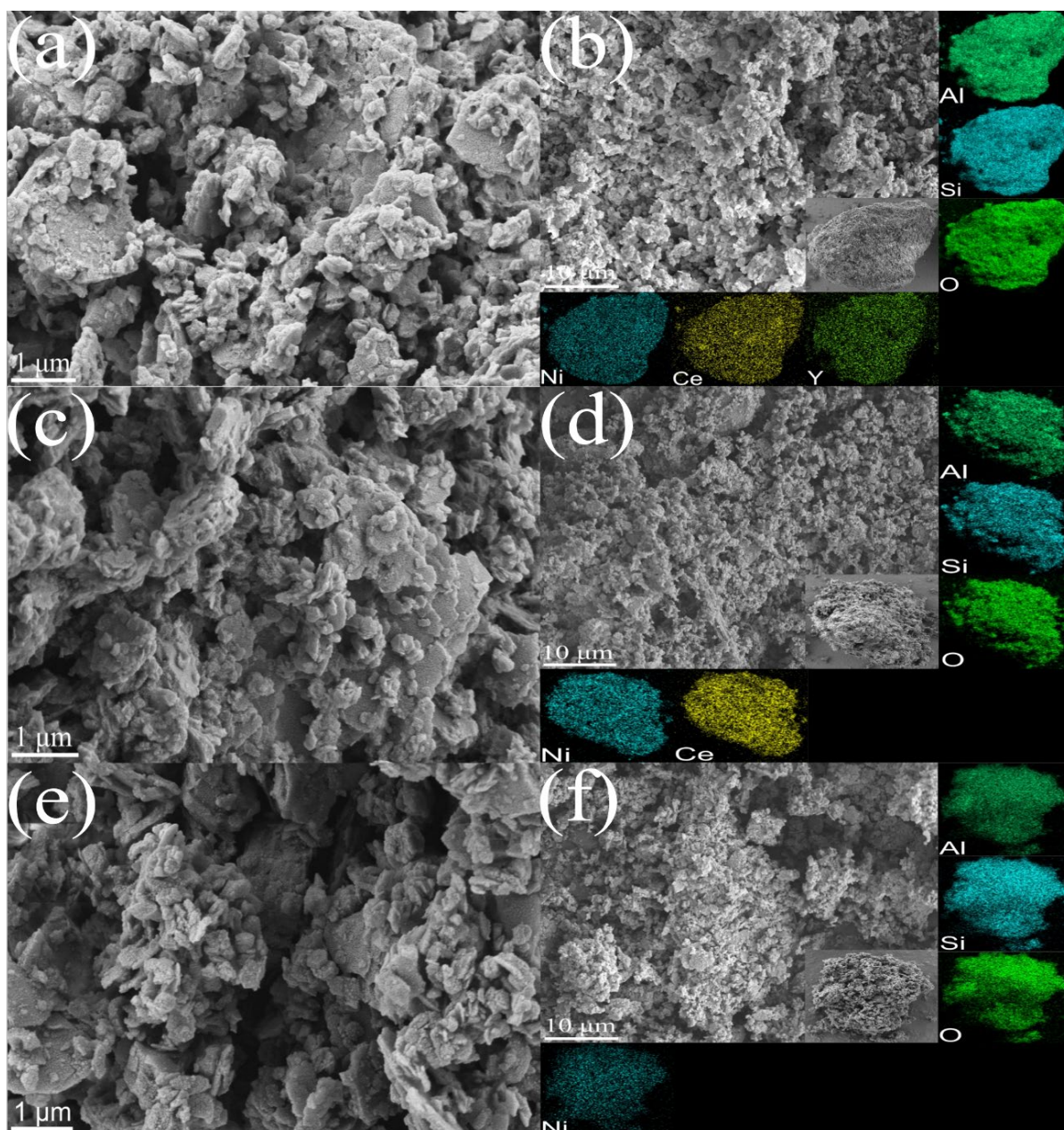


Figure 1. Corresponding BJH pore size distributions and N₂ adsorption–desorption isotherms for Ni-MK, Ce/Ni-MK, and Y-Ce/Ni-MK catalysts.

The pore structures of the Y-Ce/Ni-MK, Ce/Ni-MK, and Ni-MK samples after reduction are clearly visible in Figure 2. After incorporating active metals and promoters onto MK, the catalyst surfaces manifest a stratified morphology, which is advantageous in augmenting the specific surface area available for reactions. Furthermore, in contrast to nickel-containing catalysts documented in Table 2, the presence of smaller nickel nanoparticles in the catalysts investigated in this study suggests that MK offers a distinct advantage as a support for nickel-based catalysts compared to pure oxides. According to the EDS images, Y₂O₃, CeO₂, and nickel nanoparticles are evenly dispersed on the MK substrate, with the nickel nanoparticles demonstrating excellent dispersion on the Y-Ce/Ni-MK catalyst. Combining Figure 2f with the EDS image of the Ni-MK catalyst reveals that the porosity within the Ni-MK catalyst is blocked, and the exterior is coated with unevenly dispersed metallic nickel.

Table 1. Physicochemical attributes of Ni-MK, Ce/Ni-MK, and Y-Ce/Ni-MK.

Sample	Surface Area ($\text{m}^2 \cdot \text{g}^{-1}$)	Pore Volume ($\text{cm}^3 \cdot \text{g}^{-1}$)	Pore Diameter (nm)	Ni Loading (wt.%) ^a
Ni-MK	15.8	0.0828	20.8	13.64
Ce/Ni-MK	26.8	0.1227	18.2	12.96
Y-Ce/Ni-MK	28.3	0.1309	18.5	12.92

^a Determined by ICP-OES.**Figure 2.** SEM images of the reduced (a,b) Y-Ce/Ni-MK, (c,d) Ce/Ni-MK, and (e,f) Ni-MK catalysts.

The TEM images (Figure 3) reveal the presence of nanoscale structures in all three catalysts. A comparison between the lattice spacing observed in the HRTEM image of the reduced catalysts and the results obtained from XRD analysis confirms the existence of Ni^0 and CeO_2 . Furthermore, in the HRTEM image (Figure 3b vs. Figure 3d), the nickel metal is distinctly dispersed and surrounded by CeO_2 , indicating that the incorporation

of the Y-Ce promoter leads to a homogeneous distribution of nickel nanoparticles within the CeO_2 lattice of Y-Ce/Ni-MK [32]. Among the three catalysts, Y-Ce/Ni-MK exhibits the smallest size distribution of reduced Ni nanoparticles, measuring 5.4 nm. Furthermore, the incorporation of CeO_2 in Ce/Ni-MK results in a smaller size distribution of Ni nanoparticles (7.3 nm) compared to Ni-MK (9.2 nm). This indicates that the addition of CeO_2 causes a decrease in Ni nanoparticle size and promotes their dispersion. Additionally, the inclusion of Y_2O_3 reduces the particle size of CeO_2 [28], further promoting the dispersion of Ni nanoparticles integrated within the CeO_2 framework [32] and exerting an inhibitory effect on the movement and aggregation of the Ni nanoparticles.

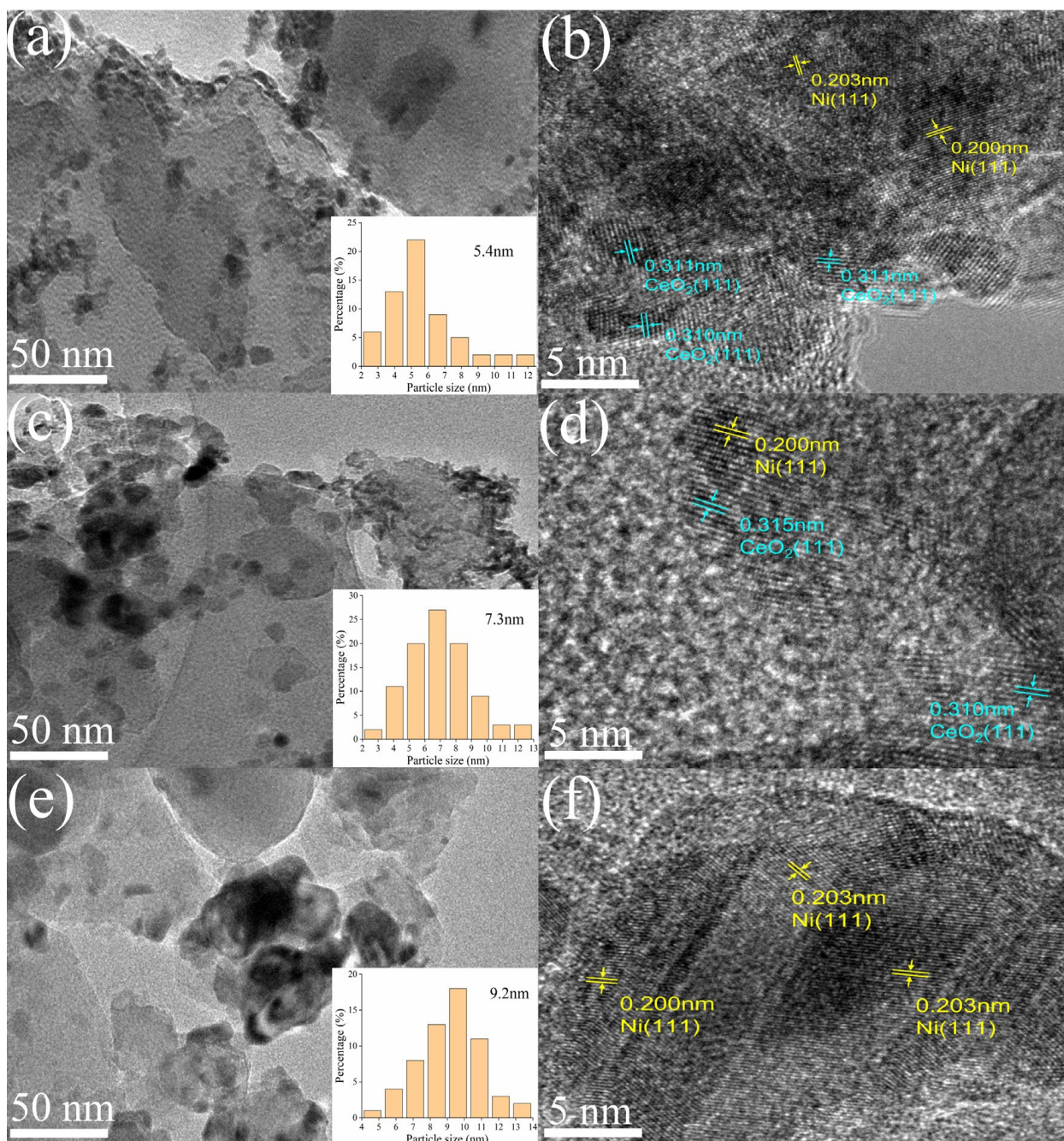


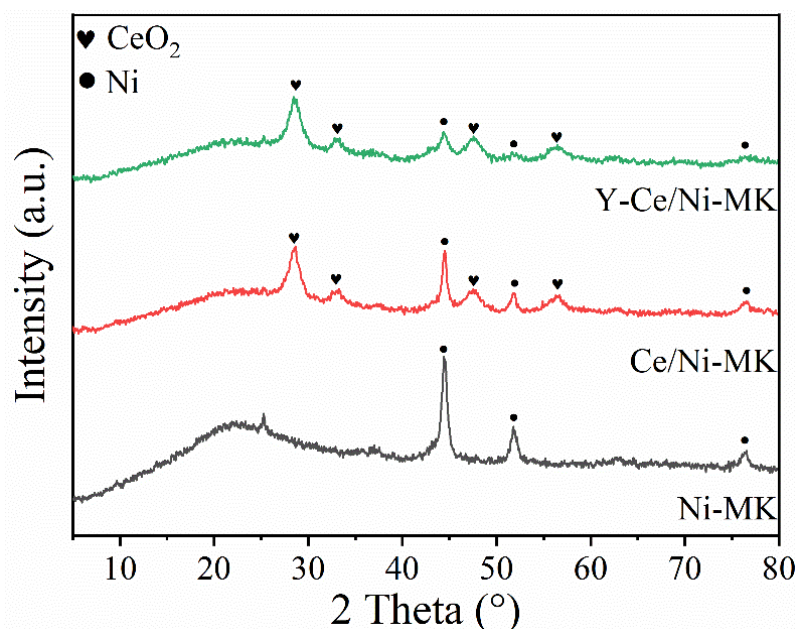
Figure 3. TEM results including mapping and HRTEM images of the reduced Y-Ce/Ni-MK (a,b), Ce/Ni-MK (c,d), and Ni-MK (e,f).

Table 2. Ni loading, Ni nanoparticles, and Ni⁰/(Ni⁰ + Ni²⁺) of various catalysts.

Catalyst	Ni Loading (wt.%)	Ni Nanoparticles (nm)	Ni ⁰ /(Ni ⁰ + Ni ²⁺)	Ref.
Ni-MK	15	9.2	5.5	This Work
Ni-CeO ₂	-	17	3.6	[33]
Ni/ZrO ₂ -E	15.1	17.46	-	[34]
15Ni/Al ₂ O ₃	15	17.2	-	[35]
Ni/Al ₂ O ₃ -P	15	12.5	-	[36]
Ni/MgO	10	12	-	[37]
Ni-P-SGS	15	13.2	-	[38]

2.2. Metal Distribution and Chemical Surface Composition of the Studied Catalysts

Based on the characterization results from wide-angle XRD, the reduced samples exhibit broad and amorphous scattering peaks, which are characteristics of highly dispersed materials. The diffraction peaks observed at 44.5°, 51.8°, and 76.4° correspond to the crystal lattice of metallic nickel (JCPDS#87-0712). Significantly, when the incorporation of metallic nickel reaches 15%, the diffraction peaks corresponding to Ni exhibit pronounced and enhanced intensity, suggesting an elevated level of crystallinity. However, upon incorporating Y metal, the strength of the Ni diffraction signals gradually diminishes, implying that the doping of Y improves the dispersibility of Ni and reduces the Ni grain size [38]. Moreover, in Figure 4, it is challenging to identify the diffraction peaks corresponding to the Y species, indicating their high dispersion on the MK matrix [39]. Meanwhile, for the Y-modified Ni/Ce-based catalyst, the diffraction peaks of CeO₂ in the 2θ range of 27° to 30° do not show significant changes upon Y doping. This suggests that the doping of Y positively affects the structural robustness of the catalyst [40]. In summary, these findings illustrate that the incorporation of Y contributes favorably to decreasing the Ni particle size and improving the dispersion of Ni.

**Figure 4.** XRD patterns of the reduced Y-Ce/Ni-MK, Ce/Ni-MK, and Ni-MK catalysts.

To assess the surface composition of the catalyst and the metal oxidation states, XPS examination was conducted on the catalyst after reduction. Illustrated in Figure 5a, the XPS graph of Ni2p_{3/2} obtained from the Y-Ce/Ni-MK catalyst exhibits Gaussian peaks positioned at 853.3, 854.5, and 856.2 eV, signifying the presence of Ni⁰, NiO, and Ni(OH)₂, in that order. The 861.5 eV peak corresponds to the shake-up satellite feature [41,42]. The

occurrence of Ni^{2+} can be linked to the incomplete oxidation of the catalyst while being exposed to air throughout the transfer process after reduction in a tubular furnace. Both Ce/Ni-MK and Ni-MK exhibit similar four peaks, but the binding energy of Y-Ce/Ni-MK is higher compared to the other two. Additionally, based on quantitative atomic energy ratio analysis (as shown in Table 3), the addition of Y_2O_3 increases the ratio of $\text{Ni}^0/(\text{Ni}^0 + \text{Ni}^{2+})$ from 5.5% to 10.2% for the Y-Ce/Ni-MK catalyst. The incorporation of Y results in an increased extent of Ni^0 reduction, enhancing the abundance of active sites and subsequently improving the catalytic activity.

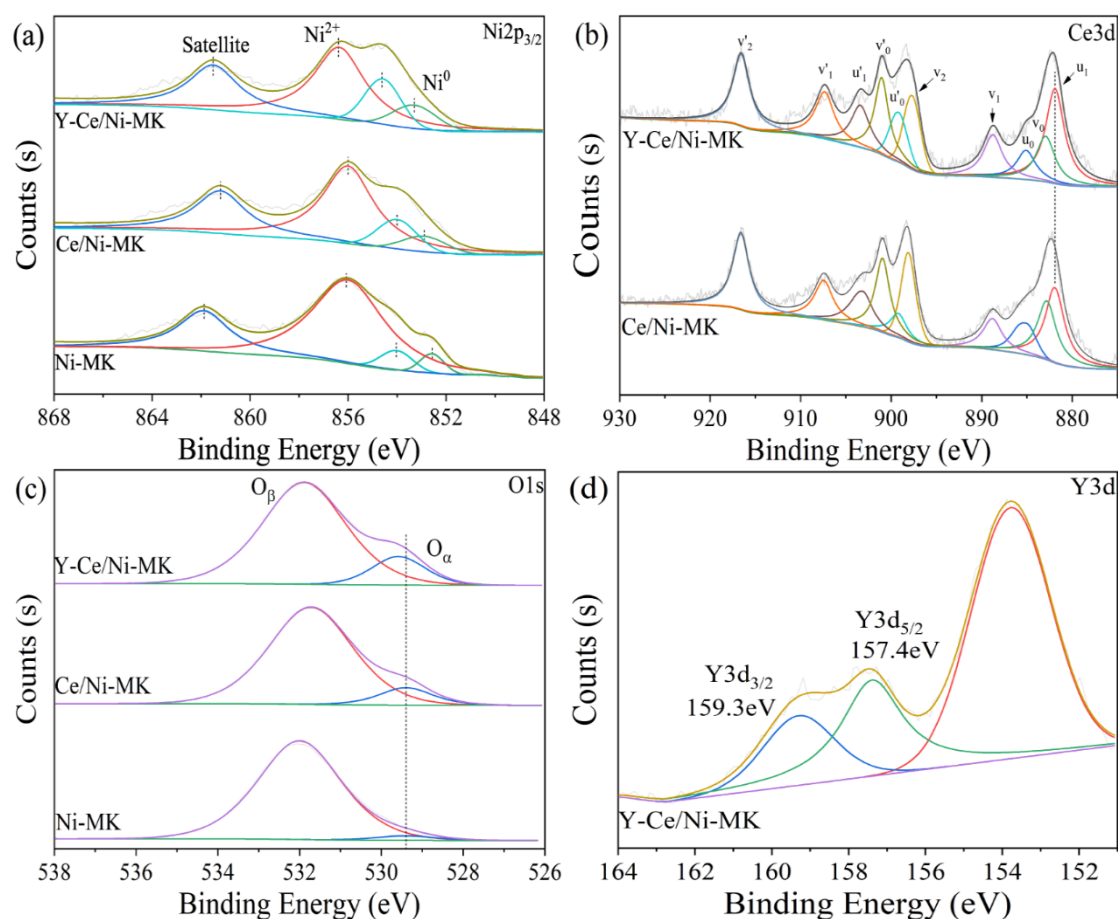


Figure 5. XPS spectra of the reduced Y-Ce/Ni-MK, Ce/Ni-MK, and Ni-MK catalysts; (a) $\text{Ni}2p_{3/2}$, (b) $\text{O}1s$, (c) $\text{Ce}3d$, (d) $\text{Y}3d$.

Table 3. XPS deconvolution results of Ni, O, and Ce.

Sample	Binding Energy(eV)				$\text{Ni}^0/(\text{Ni}^0 + \text{Ni}^{2+})$	Atomic Ratio (%)	
	$\text{Ni}2p_{3/2}$	$\text{Ce}3d_{5/2}$	$\text{O}1s$	$\text{Y}3d_{5/2}$		$\text{Ce}^{3+}/(\text{Ce}^{3+} + \text{Ce}^{4+})$	$\text{O}_\alpha/(\text{O}_\alpha + \text{O}_\beta)$
Ni-MK	856.0	—	529.4	—	5.5	—	3.9
Ce/Ni-MK	856.0	881.9	529.4	—	7.7	32.6	10.5
Y-Ce/Ni-MK	856.2	881.9	529.5	157.4	10.2	42.0	15.3

Through the process of deconvolution, it becomes possible to identify two distinct oxygen species present within the energy range of 528–533 eV, as indicated by the $\text{O}1s$ peak. The spectral region ranging from 528 to 530 eV exhibits a peak indicative of oxygen originating from the crystal lattice, denoted as O_α , while the peak observed within the energy range of 530–533 eV can be ascribed to surface oxygen that is loosely bound and chemisorbed. The examination of Table 3 reveals that the Y-Ce/Ni-MK catalyst showcases the utmost quantity of lattice oxygen. As shown in Figure 5d, the Y^{3+} species is represented

by two peaks in the Y3d orbitals at 157.4 eV (Y3d_{5/2}) and 159.3 eV (Y3d_{3/2}), consistent with other literature [40]. This indicates a weak interaction between Y and Ce, resulting in no significant peak shift for Y³⁺.

To further characterize the valence states of Ce3d, a deconvolution analysis was performed, resulting in ten peaks. Peaks u₁, u₀, u'₁, and u'₀ were assigned to Ce³⁺, while peaks v₀, v₁, v₂, v'₀, v'₁, and v'₂ were associated with Ce⁴⁺. Based on Table 3, it is evident that the Y-Ce/Ni-MK catalyst displays a higher percentage of Ce³⁺ (42.0%) compared to the Ce/Ni-MK catalyst (32.6%), indicating an increase of approximately 28.8%. This indicates that as a result of the likeness in ionic sizes between Ce and Y and their proximity, Ce⁴⁺ is substituted by Y³⁺, thereby boosting the level of Ce³⁺ and generating additional oxygen vacancies. During the reaction progression, this process positively affects the increase in Ce³⁺ concentration and the formation of additional oxygen vacancies facilitated by Y³⁺ [43]. As a result, the capacity of the carrier to reduce nickel entities is strengthened owing to the augmented quantity of oxygen vacancies, thereby resulting in enhanced catalytic activation performance.

2.3. Catalyst Reducibility and Adsorption Property

H₂-TPR experiments were conducted on the three catalysts across a temperature span from 50 to 1000 °C to investigate the interaction between Y₂O₃ and NiO, CeO₂, as well as the catalysts' reducing abilities. The H₂-TPR curves are shown in Figure 6, while Table 4 presents the peak temperatures and values for hydrogen consumption. In the graph, the Y-Ce/Ni-MK catalyst showed three reduction peaks, designated as α, β, and γ. The relatively weak γ peak appearing at (T > 800 °C) indicates the reduction of surface-bound lattice oxygen in CeO₂ [44]. The limited interaction between NiO and the MK carrier, as indicated by its larger particle size, can be attributed to the presence of the β peak, which corresponds to the reduction of NiO [33]. The infiltration of Y³⁺ or Ni²⁺ within the CeO₂ matrix, leading to the formation of Y-Ce-O or Ni-Ce-O homogeneous phases, surplus oxygen vacancies are generated. Consequently, the appearance of the α peak can be ascribed to the reduction of oxide entities attached to these vacancies [40]. With the addition of Y, the intensities of α and β peaks increase and shift towards lower temperatures. Research findings indicate a correlation between the reduction temperature and the dimensions of NiO particles, wherein smaller particle sizes correspond to reduced temperatures for the reduction process [45]. Within the context of this experiment, the introduction of Y element demonstrates a decrease in the temperature at which the main peaks undergo reduction, an augmentation in the catalyst's capability to store hydrogen, a decrease in the dimensions of NiO particles, and a reinforcement in the interplay between multimetallic species and the carrier. It is noteworthy to highlight that the hydrogen utilization associated with the α peak (as shown in Table 4) exhibits an upward trend upon the introduction of Y. Meanwhile, the hydrogen consumption corresponding to the β peak also shows a corresponding increase as a result of the heightened existence of oxygen vacancies. Nevertheless, the utilization of hydrogen for the β + γ peaks experiences an increase in the Y-Ce/Ni-MK catalyst. This suggests that Y-Ce/Ni-MK catalyst produces more oxygen vacancies in CeO₂, exhibiting stronger oxygen chemisorption capacity.

Table 4. H₂-TPR results for catalysts.

Sample	Temperature (°C)			H ₂ Consumption (μmol/g) ^a			Total H ₂ Uptake (μmol/g) ^a
	α	β	γ	α	β	γ	
Ni-MK	-	261	-	-	1654.0	-	1654.0
Ce/Ni-MK	216	259	-	486.3	1698.5	-	2184.8
Y-Ce/Ni-MK	200	251	851	687.3	1820.5	-	2507.3

^a Determined by H₂-TPR.

CO₂-TPD analyses were performed on the three catalysts to examine their surface basicity and adsorption capacity in relation to the CO₂ methanation process. By analyzing the CO₂ desorption curves, distinct temperature ranges were identified for the desorption

of CO₂: the weak region (<150 °C), the medium region (150–400 °C), and the strong region (>400 °C) [46,47]. Figure 6 illustrates the desorption behavior of CO₂ through the CO₂-TPD curves of the three catalysts. A comprehensive evaluation, involving the measurement and assessment, is provided in Table 5, presenting data on the occurrence and distribution of alkaline sites determined through the integrated desorption peaks technique [48]. According to the data in Table 5, The inclusion of Y₂O₃ leads to an increase in the overall quantity of alkaline sites present in the catalysts, and the Y-Ce/Ni-MK catalyst exhibits the highest total basicity among the three catalysts. With the addition of Y₂O₃, the following observations can be made from Table 5: (I) there is an escalation in the count of potent alkaline sites; (II) compared to the Ce/Ni-MK catalyst, there is a small reduction in the quantity of moderate alkaline sites; and (III) there is a notable rise in the quantity of weak alkaline sites. The critical role played by the coordination of moderate and weak alkaline sites in the adsorption of CO₂ is essential for enhancing its strong adsorption at low temperatures and promoting the catalyst's activity at those temperatures [49–51]. The movement of CO₂ desorption peaks to reduced temperatures in the Y-Ce/Ni-MK catalyst demonstrates the exceptional synergistic effects between Y₂O₃, CeO₂, active metallic constituents, and the MK carrier, facilitating the CO₂ activation at low temperatures [13]. To summarize, the addition of Y₂O₃ elevates the overall basicity of the catalyst, specifically augmenting the potency of moderate and weak alkaline sites, thereby amplifying the catalyst's capacity to capture and transform CO₂.

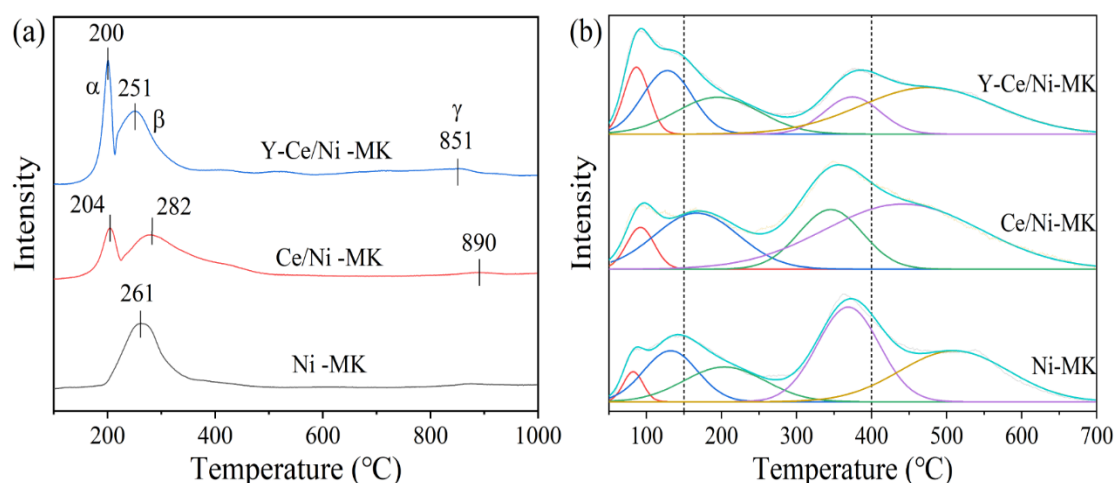


Figure 6. (a) H₂-TPR and (b) CO₂-TPD results of the reduced Y-Ce/Ni-MK, Ce/Ni-MK, and Ni-MK catalysts.

Table 5. CO₂-TPD results for catalysts.

Sample	Weak Basic Sites (μmol/g) ^a	Medium Basic Sites (μmol/g) ^a	Strong Basic Sites (μmol/g) ^a	Total Basicity (μmol/g) ^a
Ni-MK	60.5	168.3	135.8	364.6
Ce/Ni-MK	60.7	204.1	147.6	412.4
Y-Ce/Ni-MK	165.0	190.5	170.3	525.8

^a Determined by CO₂-TPD.

2.4. In Situ DRIFTS Analysis

To elucidate the working principle of the catalysts' performance, in situ DRIFTS analysis was conducted on the Y-Ce/Ni-MK, Ce/Ni-MK, and Ni-MK samples. The objective of this analysis was to examine the species involved in the methanation of CO₂ and investigate the pathways of the reaction. As shown in Figure 7, a characteristic CH₄ peak (3015 cm⁻¹) was observed for all three catalysts between 200 and 300 °C, with the peak intensity increasing with the addition of the promoter and the temperature elevation. Among them, the Y-Ce/Ni-MK catalyst exhibited the highest peak intensity,

indicating a rapid CH_4 formation. Various OH peaks were observed in the infrared spectrum between 3612 and 3800 cm^{-1} , which declined as the temperature increased. Evident from Figure 7b,c, monodentate carbonates (1417 cm^{-1} , 1328 cm^{-1}) and bidentate carbonates (1578 cm^{-1} , 1510 cm^{-1}) were observed in the spectrum, with monodentate carbonates gradually transforming into monodentate formates (1296 cm^{-1}) with increasing temperature [46,52]. The absence of substantial migration and transformation of bidentate formates within the Ce/Ni-MK and Ni-MK catalysts is apparent, indicating their resistance to conversion. As shown in Figure 7a, monodentate carbonates (1328 cm^{-1}) and bidentate carbonates (1581 cm^{-1}) of the Y-Ce/Ni-MK catalyst were observed in the spectrum, and with increasing temperature, they gradually transformed into monodentate formates (1300 cm^{-1}) and bidentate formates (1450 cm^{-1}). The reason behind this phenomenon can be traced to the elongation and flexion oscillations taking place on the initial O-C-O groups of formates [53,54]. Formates are key intermediates in the methanation process. Although the Ce/Ni-MK and Ni-MK catalysts produce monodentate formates, the conversion rate and intensity of monodentate and bidentate formates on the Y-Ce/Ni-MK catalyst exhibit a notable superiority compared to the remaining two catalysts. In conclusion, the Y-Ce/Ni-MK catalyst enhances the activity of carbonate conversion to formate and improves the ability to rapidly form CH_4 , thereby exhibiting higher catalytic activity.

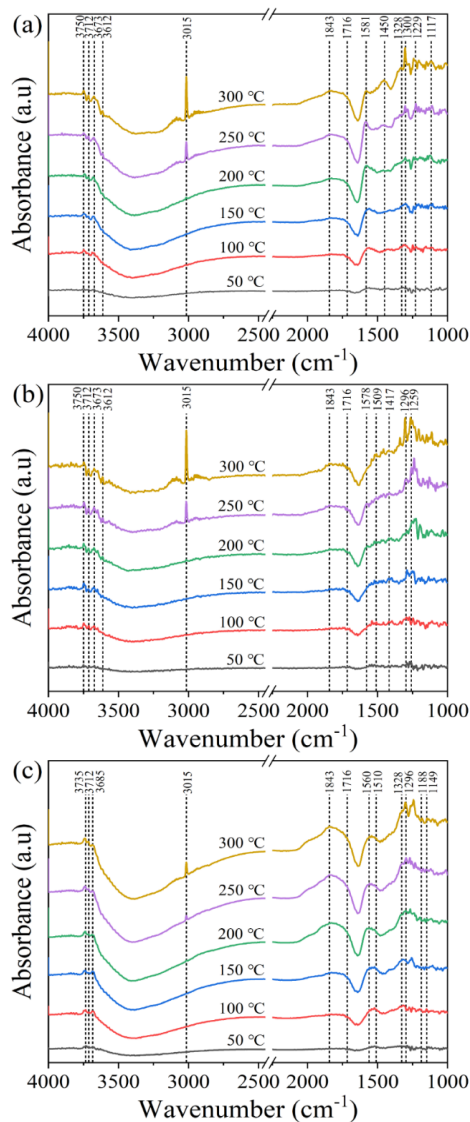
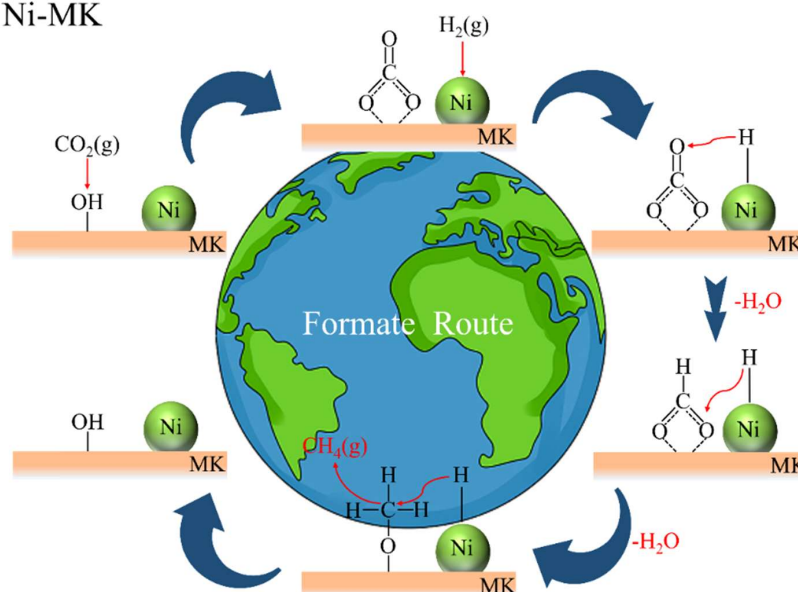


Figure 7. In situ DRIFTS investigation of CO_2 methanation over the all catalysts: (a) Y-Ce/Ni-MK, (b) Ce/Ni-MK, and (c) Ni-MK catalysts.

Based on current investigations, it has been revealed that the methanation process of CO_2 encompasses two distinct reaction pathways. One pathway entails the direct interaction between formates and H_2 , resulting in the formation of methane, while the other pathway involves the dissociation of formates into CO , followed by hydrogenation into methane [55]. However, the in situ DRIFTS measurements of the three catalysts did not exhibit any distinctive CO infrared absorption features. Consequently, our conjecture is that the reaction mechanisms of the three catalysts encompass the direct conversion of formates through hydrogenation, leading to the production of methane, as depicted in Figure 8. At the catalyst surface, CO_2 initially undergoes adsorption and reacts with hydroxyl (OH) groups, resulting in the formation of carbonates. The Ni nanoparticles attract H_2 and dissociate it into atomic hydrogen. Subsequently, the carbonates react with the atomic hydrogen to form formates and water. Finally, the formates react with hydrogen to produce methane.

(a) Ni-MK



(b) Y-Ce/Ni-MK

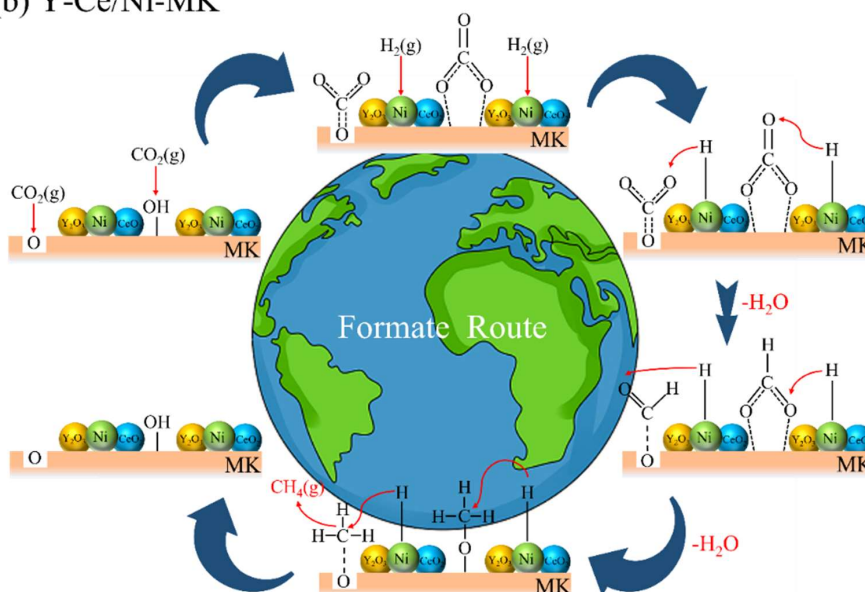


Figure 8. The main proposed pathway for CO_2 methanation over (a) Ni-MK and (b) Y-Ce/Ni-MK catalysts.

2.5. Catalytic Performance of All Catalysts and Stability Test

At a pressure of 1.0 bar and with an airflow rate of $12,000 \text{ mL} \cdot \text{g}^{-1} \cdot \text{h}^{-1}$, the performance of each catalyst was evaluated over a temperature range spanning from $250 \text{ }^\circ\text{C}$ to $450 \text{ }^\circ\text{C}$. As depicted in Table 6, Y-Ce/Ni-MK exhibits superior catalytic activity at low temperatures compared to other catalysts reported in the literature. According to the data presented in Figure 9, compared to Ce/Ni-MK and Ni-MK, the Y-Ce/Ni-MK catalyst exhibited superior activation performance with the addition of Y under conditions of reduced temperature at $300 \text{ }^\circ\text{C}$ and atmospheric pressure. At $300 \text{ }^\circ\text{C}$, the CO_2 conversion rate reached 78.4%, while the corresponding CH_4 selectivity was 99.8%. At equivalent theoretical Ni loading, the Y-modified Y-Ce/Ni-MK catalyst demonstrated enhanced catalytic efficiency, surpassing both Ce/Ni-MK and Ni-MK in terms of activity at lower operating temperatures. The achievement allowed for achieving high CO_2 conversion rates without the need for high temperatures (above $400 \text{ }^\circ\text{C}$), thereby reducing energy consumption.

Table 6. CO_2 methanation activities of various catalysts.

Catalyst	$\text{H}_2:\text{CO}_2$	Space Velocity ($\text{mL} \cdot \text{g}^{-1} \cdot \text{h}^{-1}$)	CO_2 Conversion (%)	CH_4 Selectivity (%)	Reaction Temperature ($^\circ\text{C}$)	Ref.
Y-Ce/Ni-MK	4:1	12,000	78.4	99.8	300	This Work
25Ni-5Ce- Al_2O_3	3.5:1	9000	72	98	300	[56]
Ni-CP-V2.0	4:1	12,000	68	96	300	[57]
15Ni10Ce10Y/SBA-15	4:1	12,000	20	97	300	[39]
20Ce/15Ni/CsUSY(38)	4:1	-	66	98	300	[58]
HEO-4-900/ H_2	4:1	9000	62	98	300	[59]

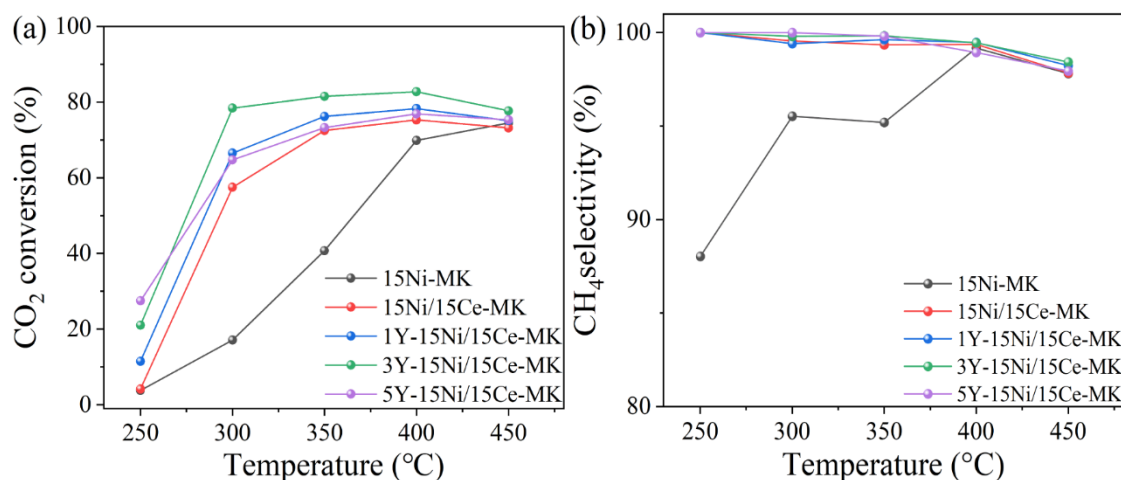


Figure 9. The Y-Ce/Ni-MK, Ce/Ni-MK, and Ni-MK catalysts synthesized in this study exhibited (a) CO_2 conversion and (b) CH_4 selectivity.

The key to achieving low-temperature high-performance with the Y-Ce/Ni-MK catalyst lies in the addition of Y_2O_3 , which enhances the concentration of oxygen vacancies, increases the strength of weak alkaline sites on the catalyst, and promotes the reactivity of CO_2 . This addition contributes positively to enhancing the CO_2 conversion efficiency. Moreover, the inclusion of Y_2O_3 restricts the diffusion of metal surface free energy, improves the dispersion of Ni, and contributes to the augmentation of catalytic performance by offering an increased number of active metal sites.

The stability over extended periods is essential for the successful commercialization of any catalyst. Therefore, stability tests were performed on the catalyst samples of Y-Ce/Ni-MK that exhibited optimal performance. The catalyst underwent a stability test for a duration of 100 h, employing the following reaction conditions: the pressure set

at 0.1 MP, the temperature maintained at 400 °C, and a flow rate of 12,000 mL·h⁻¹·g⁻¹. The catalyst's CH₄ selectivity and CO₂ conversion rate are depicted within Figure 10a. Throughout the 100 h test, the catalyst exhibited a decrease in its CO₂ conversion efficiency of approximately 3.9%, while the CH₄ selectivity exhibited no changes. Figure 10b displays the TEM image depicting the Y-Ce/Ni-MK catalyst following the 100 h stability test. Only a minor aggregation of nickel particles was observed, resulting in a rise in the mean diameter of Ni particles from 5.4 nm to 6.6 nm. In summary, the MK-based catalyst exhibits excellent stability during long-term catalysis, and the addition of Y-Ce initiators synergistically enhances the low-temperature activation performance of the MK support, while simultaneously improving the catalyst's stability over an extended duration.

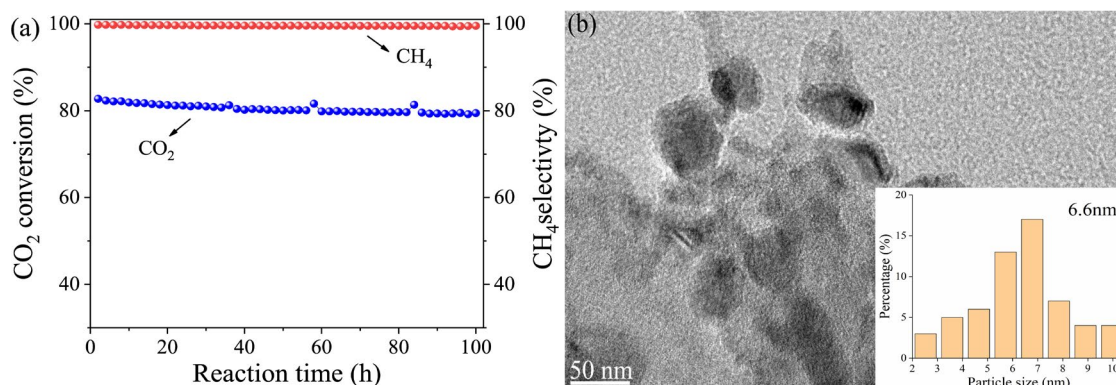


Figure 10. (a) The stability of the Y-Ce/Ni-MK catalysts over the long term; (b) HRTEM results of the reduced Y-Ce/Ni-MK.

3. Materials and Methods

3.1. Catalyst Preparation

Metakaolin, derived from kaolin clay, is a dehydrated aluminosilicate formed through constant calcination at temperatures ranging from 500 to 800 °C. Its detailed composition is listed in Table 7. The high-activity metakaolin utilized in this study was procured from Inner Mongolia Chaopai Kaolin Co., Ltd. (Togrogul Town, China), and exhibits a white appearance.

Table 7. Chemical composition of metakaolin.

Chemical Composition (Oxide)	SiO ₂	Al ₂ O ₃	Fe ₂ O ₃	K ₂ O	Na ₂ O	MgO
Metakaolin (wt.%)	48.75	42.34	0.48	0.089	0.39	0.13

The x wt% Y-Ni/Ce-MK catalysts (where x = 1, 3, 5) were synthesized using the impregnation technique, loading equimolar amounts of metal Ni and Ce onto the metakaolin (MK) support, along with varying amounts of metal Y. For convenience, these catalysts are abbreviated as xY-Ce/Ni-MK. Hexahydrated nickel nitrate (Ni(NO₃)₂·6H₂O) and hexahydrated cerium nitrate (Ce(NO₃)₃·6H₂O) (>99.0%, Macklin Chemicals, Shanghai, China) were dissolved in deionized water at room temperature. Different mass percentages of Y(NO₃)₃·6H₂O, a high-purity yttrium nitrate hexahydrate from Macklin Chemicals (>99.5%), were introduced into the aforementioned solution. The mixture was then sonicated for 15 min to attain a homogeneous dispersion. Then, the metal solution was dropped onto the MK support (5.00 g) in a beaker. The mass percentage of Y relative to Ce/Ni-MK was altered at 1, 3, and 5 wt.%, while the loading of Ni and Ce remained fixed at 15 wt.% across all catalysts. After the synthesis, the obtained samples were kept at ambient conditions for 24 h and subsequently subjected to drying at 100 °C for a duration of 24 h. The specimens were desiccated, crushed, and sifted through a 100–120 mesh sieve to acquire powders with a Y content of 3 wt.%, along with 15 wt.% Ce and 15 wt.% Ni, denoted as Y-Ce/Ni-MK. As a control experiment, Ce/Ni-MK and Ni-MK samples were synthesized

using the identical procedure, with metal loadings of 5 wt.% Ce + 15 wt.% Ni and 15 wt.% Ni, respectively.

3.2. Catalytic Activity

The catalysts were assessed for their CO₂ methanation performance in a fixed-bed reactor operating under continuous flow conditions. The operating pressure was consistently maintained at 0.1 MPa, while an embedded K-type thermocouple, located inside a stainless-steel tube, was employed as a temperature monitoring system to oversee the temperature within the catalyst bed. Placing 200 milligrams of catalyst into a fixed-bed reactor tube measuring 450 mm in length and 8 mm in width, securing the catalyst at both ends using quartz wool. Before conducting the activity tests, the samples underwent a 2 h reduction process. The samples were subjected to a reduction process at a temperature of 500 °C and a pressure of 0.1 MPa. This process involved exposing the samples to a gas mixture containing H₂ and N₂, with a molar ratio of 1:9. (space velocity, WHSV = 12,000 mL g⁻¹ h⁻¹). Once the catalysts were cooled to ambient temperature, a methane reaction was conducted using a feed gas with a CO₂/H₂ ratio of 1:4. The gas product composition at the exit was evaluated by means of a gas analyzer furnished with a thermal conductivity detector (GC9800), and the amounts of each component gas were measured. To investigate the catalyst activity, the temperature range of 200 °C to 450 °C was employed during the experimental procedure. After a 30 min dwelling time at each 50 °C interval, stable measurements were obtained by introducing the samples. The gas compositions at the outlet were analyzed using an internal reference technique.

The catalyst's efficiency was evaluated based on its effectiveness in converting CO₂ and selecting CH₄. The ratio of consumed CO₂ to the initial CO₂ feedstock during the reaction was used to calculate the CO₂ conversion efficiency. The calculation for the CH₄ selectivity and CO₂ conversion rate was as outlined below:

$$X_{\text{CO}_2} = \frac{n_{\text{CO}_2}^{\text{in}} - n_{\text{CO}_2}^{\text{out}}}{n_{\text{CO}_2}^{\text{in}}} \times 100\% \quad (2)$$

$$S_{\text{CH}_4} = \frac{n_{\text{CH}_4}^{\text{in}}}{n_{\text{CH}_4}^{\text{out}} + n_{\text{CH}_4}^{\text{in}}} \times 100\% \quad (3)$$

where $n_{\text{CO}_2}^{\text{in}}$ represents the CO₂ flow rate within the feed-stream, and $n_{\text{CO}_2}^{\text{out}}$ and $n_{\text{CH}_4}^{\text{out}}$ indicate the flow velocities of CO₂ and CH₄ within the reformed gas at the outlet.

3.3. Catalyst Characterization

X-ray diffraction (XRD) analysis was conducted on the catalysts utilizing a Rigaku MiniFlex 600 instrument (Tokyo, Japan) for diffraction measurements, with emitted radiation source of Cu-K α (a wavelength of 0.154 nm). It operated with a voltage of 40 kV and a current of 15 mA. The span of measurement, encompassing from 20° to 80°, was selected, employing a step size of 5° per minute.

To determine the actual concentrations of Ni, Ce, and Y within the catalyst, inductively coupled plasma optical emission spectroscopy (ICPOES) was performed using an Agilent 720ES(OES) instrument (Santa Clara, CA, USA).

The catalyst samples underwent an 8 h pretreatment in a Micromeritics APSP 2460 (Norcross, GA, USA) degassing station at 300 °C under vacuum. Subsequently, the measurement of nitrogen adsorption–desorption isotherms was conducted using the same instrument at 77 K (liquid nitrogen temperature). To determine the overall specific surface area of the catalyst, the obtained isotherms were analyzed using the Brunauer–Emmett–Teller (BET) technique. The Barrett–Joyner–Halenda (BJH) technique was employed for the calculation of the pore size and pore volume of the samples.

The Micromeritics AutoChem II 2920 device (Norcross, GA, USA) was utilized to perform the hydrogen thermal ramp reduction (H₂-TPR) experiment. Initially, the catalyst was subjected to drying and pretreatment at 300 °C with a catalyst mass of 30 mg.

Subsequently, the catalyst underwent a helium flow (50 mL/min) for a duration of 1 h, followed by cooling it down to 50 °C. After that, in the presence of a flow of 10% H₂/Ar (50 mL/min), the specimen was subjected to a temperature ramping process at a rate of 10 °C/min, reaching up to 1000 °C during desorption.

The CO₂ temperature-programmed desorption (CO₂-TPD) tests were performed using the Micromeritics AutoChem II 2920 instrument. Initially, a 50 mg catalyst sample was carefully weighed and introduced into the reaction tube. Subsequently, the catalyst underwent a drying pretreatment by gradually increasing the temperature from ambient conditions to 300 °C. After a duration of 1 h, the system was subsequently cooled down to 50 °C while a helium flow (30–50 mL/min) was directed over the catalyst. Subsequently, a blend comprising carbon dioxide and helium gas (30–50 mL/min) was introduced for 1 h until saturation, after which the helium flow (30–50 mL/min) was switched to remove weakly adsorbed CO₂ on the catalyst surface for 1 h. In the final step, with a controlled increment of 10 °C per minute, the temperature was raised to 700 °C in the presence of a helium environment. During this process, by utilizing a thermal conductivity detector (TCD), the desorption profiles were recorded, ensuring precise temperature monitoring and collection of desorption data.

X-ray photoelectron spectroscopy (XPS; Thermo Scientific K-Alpha; Al K α X-ray source) was employed to calibrate the oxidation states of each element, using C1s at 284.8 eV as the reference.

A field-emission scanning electron microscope (FE-SEM) model SU8220 from Hitachi (Tokyo, Japan), along with an energy-dispersive X-ray spectroscopy (EDX) system provided by Bruker, was employed for scanning analysis and elemental composition analysis of the reduced catalyst.

Using a FEI 80-300 (West Springfield, MA, USA) Titan (S) transmission electron microscope (HRTEM) operating at 300 kV, the catalyst samples were inspected to observe their morphology, and the size of metal particles was determined through the utilization of the Nano Measurer (1.2) software.

During the reaction, the formation of intermediate species was investigated, in situ diffuse reflectance Fourier-transform infrared spectroscopy (DRIFTS) was utilized. Using a Nicolet IS 50 spectrometers equipped with a cryogenically cooled MCT detector, in situ DRIFTS measurements were conducted. Before conducting the measurements, the sample was subjected to a reduction process at a temperature of 500 °C for a period of 2 h, during which it was subjected to a stream of hydrogen (30 mL min⁻¹). The sample, which had undergone reduction, weighing 5 mg, was positioned on the sample holder, precisely at the midpoint of the sample pool. Afterward, a blend of carbon dioxide and hydrogen was introduced, and the thermal condition was elevated at a speed of 5 °C per minute until reaching 300 °C, with an infrared spectrum captured at every 50 °C increment.

4. Conclusions

In this study, a novel Y-Ce/Ni-MK catalyst was synthesized by employing metakaolin as a support via the co-impregnation method. The inclusion of yttrium (Y) had beneficial effects, promoting the creation of oxygen vacancies and alkaline sites. This played a pivotal role in improving the reducibility of nickel species, enhancing nickel particle dispersion, and increasing thermal stability. The catalyst demonstrated outstanding catalytic performance at approximately 300 °C and retained its high activity throughout a 100 h stability test. These results underscore the substantial potential of environmentally friendly, cost-effective metakaolin-supported nickel-based catalysts. These catalysts, prepared using a straightforward method, are promising for CO₂ methanation at lower temperatures. The investigation unveiled synergistic interactions between the Y-Ce promoter, the Ni catalyst, and the metakaolin substrate, resulting in increased activity in the CO₂ methanation reaction. This study provides an economical and straightforward method for producing stable catalysts for CO₂ methanation, characterized by high activity. It explores the potential of synergistic catalysis involving multiple metals and metakaolin support, offering a

greener, more environmentally friendly, and cost-efficient alternative for industrial CO₂ methanation applications.

Author Contributions: Experiment, investigation, writing—original draft, methodology, validation, Y.W.; software, Q.Y.; formal analysis, X.X.; supervision, investigation, A.S.D.; writing—review and editing, project administration, funding acquisition, X.C. All authors have read and agreed to the published version of the manuscript.

Funding: This work was supported by the Chinese Natural Science Fund (Grant: 51772055) and the Guangxi Natural Science Fund (grant: 2022GXNSFDA035062). Innovation Project of Guangxi Graduate Education (Grant: YCSW2023092).

Institutional Review Board Statement: Not applicable.

Informed Consent Statement: Not applicable.

Data Availability Statement: Not applicable.

Acknowledgments: This work was supported by the Chinese Natural Science Fund (Grant: 51772055) and the Guangxi Natural Science Fund (grant: 2022GXNSFDA035062). Innovation Project of Guangxi Graduate Education (Grant: YCSW2023092).

Conflicts of Interest: The authors declare no conflict of interest.

Sample Availability: Not applicable.

References

1. Pham, C.Q.; Bahari, M.B.; Kumar, P.S.; Ahmed, S.F.; Xiao, L.; Kumar, S.; Qazaq, A.S.; Siang, T.J.; Tran, H.-T.; Islam, A.; et al. Carbon dioxide methanation on heterogeneous catalysts: A review. *Environ. Chem. Lett.* **2022**, *20*, 3613–3630. [[CrossRef](#)]
2. Porosoff, M.D.; Yan, B.; Chen, J.G. Catalytic reduction of CO₂ by H₂ for synthesis of CO, methanol and hydrocarbons: Challenges and opportunities. *Energy Environ. Sci.* **2016**, *9*, 62–73. [[CrossRef](#)]
3. Senftle, T.P.; Carter, E.A. The Holy Grail: Chemistry Enabling an Economically Viable CO₂ Capture, Utilization, and Storage Strategy. *Acc. Chem. Res.* **2017**, *50*, 472–475. [[CrossRef](#)]
4. Rodemerck, U.; Holeňa, M.; Wagner, E.; Smejkal, Q.; Barkschat, A.; Baerns, M. Catalyst Development for CO₂ Hydrogenation to Fuels. *ChemCatChem* **2013**, *5*, 1948–1955. [[CrossRef](#)]
5. Mod, E.C.; Roy, S.; Ernst, J.; Kharchenko, P.V.; Kheradpour, P.; Negre, N.; Eaton, M.L.; Landolin, J.M.; Bristow, C.A.; Ma, L.; et al. Identification of functional elements and regulatory circuits by *Drosophila* mod ENCODE. *Science* **2010**, *330*, 1787–1797.
6. Sarić, M.; Dijkstra, J.W.; Haije, W.G. Economic perspectives of Power-to-Gas technologies in bio-methane production. *J. CO₂ Util.* **2017**, *20*, 81–90. [[CrossRef](#)]
7. Lin, Q.; Liu, X.Y.; Jiang, Y.; Wang, Y.; Huang, Y.; Zhang, T. Crystal phase effects on the structure and performance of ruthenium nanoparticles for CO₂ hydrogenation. *Catal. Sci. Technol.* **2014**, *4*, 2058–2063. [[CrossRef](#)]
8. Beaumont, S.K.; Alayoglu, S.; Pushkarev, V.V.; Liu, Z.; Kruse, N.; Somorjai, G.A. Exploring surface science and restructuring in reactive atmospheres of colloidal prepared bimetallic CuNi and CuCo nanoparticles on SiO₂ in situ using ambient pressure X-ray photoelectron spectroscopy. *Faraday Discuss.* **2013**, *162*, 31–44. [[CrossRef](#)]
9. Yang, Y.; Liu, J.; Liu, F.; Wu, D. Reaction mechanism of CO₂ methanation over Rh/TiO₂ catalyst. *Fuel* **2020**, *276*, 118093. [[CrossRef](#)]
10. Chen, B.; Qiu, J.; Xu, L.; Cui, Y. Ni-based mesoporous Ce_{0.8}Zr_{0.2}O₂ catalyst with enhanced low-temperature performance for CO₂ methanation. *Catal. Commun.* **2022**, *171*, 106515. [[CrossRef](#)]
11. Matsumura, Y.; Ishibe, H. Durable copper–zinc catalysts modified with indium oxide in high temperature steam reforming of methanol for hydrogen production. *J. Power Sources* **2012**, *209*, 72–80. [[CrossRef](#)]
12. Lorenz, H.; Jochum, W.; Klötzer, B.; Stöger-Pollach, M.; Schwarz, S.; Pfaller, K.; Penner, S. Novel methanol steam reforming activity and selectivity of pure In₂O₃. *Appl. Catal. A Gen.* **2008**, *347*, 34–42. [[CrossRef](#)]
13. Wang, X.; Zhu, L.; Liu, Y.; Wang, S. CO₂ methanation on the catalyst of Ni/MCM-41 promoted with CeO₂. *Sci. Total Environ.* **2018**, *625*, 686–695. [[CrossRef](#)] [[PubMed](#)]
14. Graça, I.; González, L.V.; Bacariza, M.C.; Fernandes, A.; Henriques, C.; Lopes, J.M.; Ribeiro, M.F. CO₂ hydrogenation into CH₄ on NiHNaUSY zeolites. *Appl. Catal. B: Environ.* **2014**, *147*, 101–110. [[CrossRef](#)]
15. Xu, J.; Su, X.; Duan, H.; Hou, B.; Lin, Q.; Liu, X.; Pan, X.; Pei, G.; Geng, H.; Huang, Y.; et al. Influence of pretreatment temperature on catalytic performance of rutile TiO₂-supported ruthenium catalyst in CO₂ methanation. *J. Catal.* **2016**, *333*, 227–237. [[CrossRef](#)]
16. Garbarino, G.; Bellotti, D.; Finocchio, E.; Magistri, L.; Busca, G. Methanation of carbon dioxide on Ru/Al₂O₃: Catalytic activity and infrared study. *Catal. Today* **2016**, *277*, 21–28. [[CrossRef](#)]
17. Ren, J.; Zeng, F.; Mebrahtu, C.; Palkovits, R. Understanding promotional effects of trace oxygen in CO₂ methanation over Ni/ZrO₂ catalysts. *J. Catal.* **2022**, *405*, 385–390. [[CrossRef](#)]

18. Preianò, M.; Pasqua, L.; Gallelli, L.; Galasso, O.; Gasparini, G.; Savino, R.; Terracciano, R. Simultaneous extraction and rapid visualization of peptidomic and lipidomic body fluids fingerprints using mesoporous aluminosilicate and MALDI-TOF MS. *Proteomics* **2012**, *12*, 3286–3294. [[CrossRef](#)]
19. Sholeha, N.A.; Jannah, L.; Rohma, H.N.; Widiastuti, N.; Prasetyoko, D.; Jalil, A.A.; Bahruji, H. Synthesis of Zeolite NaY from Dealuminated Metakaolin as Ni Support for CO₂ Hydrogenation to Methane. *Clays Clay Miner.* **2020**, *68*, 513–523. [[CrossRef](#)]
20. Chouikhi, N.; Cecilia, J.A.; Vilarrasa-García, E.; Besghaier, S.; Chlendi, M.; Franco Duro, F.I.; Rodriguez Castellon, E.; Bagane, M. CO₂ Adsorption of Materials Synthesized from Clay Minerals: A Review. *Minerals* **2019**, *9*, 514. [[CrossRef](#)]
21. Li, D.; Zeng, L.; Li, X.; Wang, X.; Ma, H.; Assabumrungrat, S.; Gong, J. Ceria-promoted Ni/SBA-15 catalysts for ethanol steam reforming with enhanced activity and resistance to deactivation. *Appl. Catal. B Environ.* **2015**, *176–177*, 532–541. [[CrossRef](#)]
22. Baysal, Z.; Kureti, S. CO₂ methanation on Mg-promoted Fe catalysts. *Appl. Catal. B Environ.* **2020**, *262*, 118300. [[CrossRef](#)]
23. Bacariza, M.C.; Graça, I.; Bebiano, S.S.; Lopes, J.M.; Henriques, C. Magnesium as Promoter of CO₂ Methanation on Ni-Based USY Zeolites. *Energy Fuels* **2017**, *31*, 9776–9789. [[CrossRef](#)]
24. Li, J.F.; Xia, C.; Au, C.T.; Liu, B.S. Y₂O₃-promoted NiO/SBA-15 catalysts highly active for CO₂/CH₄ reforming. *Int. J. Hydrog. Energy* **2014**, *39*, 10927–10940. [[CrossRef](#)]
25. Romero-Sáez, M.; Dongil, A.B.; Benito, N.; Espinoza-González, R.; Escalona, N.; Gracia, F. CO₂ methanation over nickel-ZrO₂ catalyst supported on carbon nanotubes: A comparison between two impregnation strategies. *Appl. Catal. B Environ.* **2018**, *237*, 817–825. [[CrossRef](#)]
26. Lin, J.; Ma, C.; Wang, Q.; Xu, Y.; Ma, G.; Wang, J.; Wang, H.; Dong, C.; Zhang, C.; Ding, M. Enhanced low-temperature performance of CO₂ methanation over mesoporous Ni/Al₂O₃-ZrO₂ catalysts. *Appl. Catal. B Environ.* **2019**, *243*, 262–272. [[CrossRef](#)]
27. Sun, C.; Świrk Da Costa, K.; Wierzbicki, D.; Motak, M.; Grzybek, T.; Da Costa, P. On the effect of yttrium promotion on Ni-layered double hydroxides-derived catalysts for hydrogenation of CO₂ to methane. *Int. J. Hydrog. Energy* **2021**, *46*, 12169–12179. [[CrossRef](#)]
28. Battumur, N.; Sergelenbaatar, N.; Bold, T.; Byambajav, E. Cerium-promoted nickel catalysts supported on yttrium-doped γ -alumina for carbon dioxide methanation. *J. CO₂ Util.* **2023**, *68*, 102380. [[CrossRef](#)]
29. Qin, Z.; Wang, X.; Dong, L.; Su, T.; Li, B.; Zhou, Y.; Jiang, Y.; Luo, X.; Ji, H. CO₂ methanation on Co/TiO₂ catalyst: Effects of Y on the support. *Chem. Eng. Sci.* **2019**, *210*, 115245. [[CrossRef](#)]
30. Albarazi, A.; Beaunier, P.; Da Costa, P. Hydrogen and syngas production by methane dry reforming on SBA-15 supported nickel catalysts: On the effect of promotion by Ce_{0.75}Zr_{0.25}O₂ mixed oxide. *Int. J. Hydrog. Energy* **2013**, *38*, 127–139. [[CrossRef](#)]
31. Liu, C.; Zhou, J.; Ma, H.; Qian, W.; Zhang, H.; Ying, W. Antisintering and High-Activity Ni Catalyst Supported on Mesoporous Silica Incorporated by Ce/Zr for CO Methanation. *Ind. Eng. Chem. Res.* **2018**, *57*, 14406–14416. [[CrossRef](#)]
32. Ye, R.-P.; Li, Q.; Gong, W.; Wang, T.; Razink, J.J.; Lin, L.; Qin, Y.-Y.; Zhou, Z.; Adidharma, H.; Tang, J.; et al. High-performance of nanostructured Ni/CeO₂ catalyst on CO₂ methanation. *Appl. Catal. B Environ.* **2020**, *268*, 118474. [[CrossRef](#)]
33. Yu, Y.; Chan, Y.M.; Bian, Z.; Song, F.; Wang, J.; Zhong, Q.; Kawi, S. Enhanced performance and selectivity of CO₂ methanation over g-C₃N₄ assisted synthesis of Ni CeO₂ catalyst: Kinetics and DRIFTS studies. *Int. J. Hydrog. Energy* **2018**, *43*, 15191–15204. [[CrossRef](#)]
34. Zhao, K.; Wang, W.; Li, Z. Highly efficient Ni/ZrO₂ catalysts prepared via combustion method for CO₂ methanation. *J. CO₂ Util.* **2016**, *16*, 236–244. [[CrossRef](#)]
35. Rahmani, S.; Rezaei, M.; Meshkani, F. Preparation of highly active nickel catalysts supported on mesoporous nanocrystalline γ -Al₂O₃ for CO₂ methanation. *J. Ind. Eng. Chem.* **2014**, *20*, 1346–1352. [[CrossRef](#)]
36. Sun, J.; Wang, Y.; Zou, H.; Guo, X.; Wang, Z.-J. Ni catalysts supported on nanosheet and nanoplate γ -Al₂O₃ for carbon dioxide methanation. *J. Energy Chem.* **2019**, *29*, 3–7. [[CrossRef](#)]
37. Jing, J.-Y.; Yang, Z.-F.; Huo, J.-M.; Bai, H.-C.; Li, W.-Y. Metal precursor impregnation sequence effect on the structure and performance of Ni Co/MgO catalyst. *Int. J. Hydrog. Energy* **2019**, *44*, 8089–8098. [[CrossRef](#)]
38. Wan, H.; He, Y.; Su, Q.; Liu, L.; Cui, X. Slag-based geopolymer microspheres as a support for CO₂ methanation. *Fuel* **2022**, *319*, 123627. [[CrossRef](#)]
39. Sun, C.; Świrk Da Costa, K.; Wang, Y.; Scheidl, K.S.; Breiby, D.W.; Rønning, M.; Hu, C.; Da Costa, P. Tailoring the yttrium content in Ni-Ce-Y/SBA-15 mesoporous silicas for CO₂ methanation. *Catal. Today* **2021**, *382*, 104–119. [[CrossRef](#)]
40. Sun, C.; Beaunier, P.; La Parola, V.; Liotta, L.F.; Da Costa, P. Ni/CeO₂ Nanoparticles Promoted by Yttrium Doping as Catalysts for CO₂ Methanation. *ACS Appl. Nano Mater.* **2020**, *3*, 12355–12368. [[CrossRef](#)]
41. Németh, M.; Schay, Z.; Srankó, D.; Károlyi, J.; Sáfrán, G.; Sajó, I.; Horváth, A. Impregnated Ni/ZrO₂ and Pt/ZrO₂ catalysts in dry reforming of methane: Activity tests in excess methane and mechanistic studies with labeled ¹³CO₂. *Appl. Catal. A Gen.* **2015**, *504*, 608–620. [[CrossRef](#)]
42. Singha, R.K.; Shukla, A.; Yadav, A.; Adak, S.; Iqbal, Z.; Siddiqui, N.; Bal, R. Energy efficient methane tri-reforming for synthesis gas production over highly coke resistant nanocrystalline Ni-ZrO₂ catalyst. *Appl. Energy* **2016**, *178*, 110–125. [[CrossRef](#)]
43. Du, X.; Zhang, D.; Shi, L.; Gao, R.; Zhang, J. Morphology Dependence of Catalytic Properties of Ni/CeO₂ Nanostructures for Carbon Dioxide Reforming of Methane. *J. Phys. Chem. C* **2012**, *116*, 10009–10016. [[CrossRef](#)]
44. Atribak, I.; Bueno-Lopez, A.; Garcia-Garcia, A. Role of yttrium loading in the physico-chemical properties and soot combustion activity of ceria and ceria-zirconia catalysts. *J. Mol. Catal. A-Chem.* **2009**, *300*, 103–110. [[CrossRef](#)]

45. Singha, R.K.; Shukla, A.; Yadav, A.; Sivakumar Konathala, L.N.; Bal, R. Effect of metal-support interaction on activity and stability of Ni-CeO₂ catalyst for partial oxidation of methane. *Appl. Catal. B Environ.* **2017**, *202*, 473–488. [[CrossRef](#)]
46. Jia, X.; Zhang, X.; Rui, N.; Hu, X.; Liu, C.-J. Structural effect of Ni/ZrO₂ catalyst on CO₂ methanation with enhanced activity. *Appl. Catal. B Environ.* **2019**, *244*, 159–169. [[CrossRef](#)]
47. Li, Y.; Men, Y.; Liu, S.; Wang, J.; Wang, K.; Tang, Y.; An, W.; Pan, X.; Li, L. Remarkably efficient and stable Ni/Y₂O₃ catalysts for CO₂ methanation: Effect of citric acid addition. *Appl. Catal. B Environ.* **2021**, *293*, 120206. [[CrossRef](#)]
48. Coleman, L.J.I.; Epling, W.; Hudgins, R.R.; Croiset, E. Ni/Mg–Al mixed oxide catalyst for the steam reforming of ethanol. *Appl. Catal. A Gen.* **2009**, *363*, 52–63. [[CrossRef](#)]
49. Chen, X.; He, Y.; Cui, X.; Liu, L. High value utilization of waste blast furnace slag: New Ni-CeO₂/hBFS catalyst for low temperature CO₂ methanation. *Fuel* **2023**, *338*, 127309. [[CrossRef](#)]
50. Lee, S.M.; Lee, Y.H.; Moon, D.H.; Ahn, J.Y.; Nguyen, D.D.; Chang, S.W.; Kim, S.S. Reaction Mechanism and Catalytic Impact of Ni/CeO_{2-x} Catalyst for Low-Temperature CO₂ Methanation. *Ind. Eng. Chem. Res.* **2019**, *58*, 8656–8662. [[CrossRef](#)]
51. Tan, M.; Wang, X.; Wang, X.; Zou, X.; Ding, W.; Lu, X. Influence of calcination temperature on textural and structural properties, reducibility, and catalytic behavior of mesoporous γ -alumina-supported Ni–Mg oxides by one-pot template-free route. *J. Catal.* **2015**, *329*, 151–166. [[CrossRef](#)]
52. Saw, E.T.; Oemar, U.; Tan, X.R.; Du, Y.; Borgna, A.; Hidajat, K.; Kawi, S. Bimetallic Ni–Cu catalyst supported on CeO₂ for high-temperature water–gas shift reaction: Methane suppression via enhanced CO adsorption. *J. Catal.* **2014**, *314*, 32–46. [[CrossRef](#)]
53. Panagiotopoulou, P. Methanation of CO₂ over alkali-promoted Ru/TiO₂ catalysts: II. Effect of alkali additives on the reaction pathway. *Appl. Catal. B Environ.* **2018**, *236*, 162–170. [[CrossRef](#)]
54. Marwood, M.; Doepper, R.; Renken, A. In-situ surface and gas phase analysis for kinetic studies under transient conditions the catalytic hydrogenation of CO₂. *Appl. Catal. A Gen.* **1997**, *151*, 223–246. [[CrossRef](#)]
55. Westermann, A.; Azambre, B.; Bacariza, M.C.; Graça, I.; Ribeiro, M.F.; Lopes, J.M.; Henriques, C. Insight into CO₂ methanation mechanism over NiUSY zeolites: An operando IR study. *Appl. Catal. B Environ.* **2015**, *174–175*, 120–125. [[CrossRef](#)]
56. Daroughegi, R.; Meshkani, F.; Rezaei, M. Enhanced low-temperature activity of CO₂ methanation over ceria-promoted Ni-Al₂O₃ nanocatalyst. *Chem. Eng. Sci.* **2021**, *230*, 116194. [[CrossRef](#)]
57. Summa, P.; Swirk, K.; Wierzbicki, D.; Motak, M.; Alxneit, I.; Ronning, M.; Da Costa, P. Co-Precipitated Ni-Mg-Al Hydrotalcite-Derived Catalyst Promoted with Vanadium for CO₂ Methanation. *Molecules* **2021**, *26*, 6506. [[CrossRef](#)]
58. Bacariza, M.C.; Graça, I.; Lopes, J.M.; Henriques, C. Ni-Ce/Zeolites for CO₂ Hydrogenation to CH₄: Effect of the Metal Incorporation Order. *ChemCatChem* **2018**, *10*, 2773–2781. [[CrossRef](#)]
59. Liao, Y.; He, Y.; Cui, X.; Liu, L. Elemental Fe conditioning for the synthesis of highly selective and stable high entropy catalysts for CO₂ methanation. *Fuel* **2023**, *355*, 129494. [[CrossRef](#)]

Disclaimer/Publisher’s Note: The statements, opinions and data contained in all publications are solely those of the individual author(s) and contributor(s) and not of MDPI and/or the editor(s). MDPI and/or the editor(s) disclaim responsibility for any injury to people or property resulting from any ideas, methods, instructions or products referred to in the content.